Journal of Geophysical Research: Atmospheres

RESEARCH ARTICLE
10.1029/2017JD027927

Special Section:
Quantifying the emission, properties, and diverse impacts of wildfire smoke

Satellite-Observed Impacts of Wildfires on Regional Atmosphere Composition and the Shortwave Radiative Forcing: A Multiple Case Study

Yuyun Fu[1], Rui Li[1], Jianguo Huang[2], Yves Bergeron[3], Yunfei Fu[1], Yu Wang[1], and Zongting Gao[4]

[1]School of Earth and Space Sciences, University of Science and Technology of China, Hefei, China, [2]Key Laboratory of Vegetation Restoration and Management of Degraded Ecosystems, Guangdong Provincial Key Laboratory of Applied Botany, South China Botanical Garden, Chinese Academy of Sciences, Guangzhou, China, [3]Institut de recherche sur les forêts, Université du Québec en Abitibi-Témiscamingue (UQAT), Rouyn-Noranda, Quebec, Canada, [4]Institute of Meteorological Sciences of Jilin Province, Jilin Provincial Key Laboratory of Changbai Mountain Meteorology and Climate Change, Laboratory of Research for Middle-High Latitude Circulation and East Asian Monsoon, Changchun, China

Key Points:
- Satellite-retrieved fire radiative power can be used to estimate the emission coefficients of smoke and multiple trace gases from wildfires
- Cropland fire case shows lower aerosol and carbon monoxide but much higher nitrogen oxides emission coefficients than those of forest fires
- Shortwave radiative forcing coefficients are similar among multiple fire cases despite the different fuel type and emissions

Supporting Information:
- Supporting Information S1

Correspondence to:
R. Li,
rli7@ustc.edu.cn

Citation:
Fu, Y., Li, R., Huang, J., Bergeron, Y., Fu, Y., Wang, Y., & Gao, Z. (2018). Satellite-observed impacts of wildfires on regional atmosphere composition and the shortwave radiative forcing: A multiple case study. *Journal of Geophysical Research: Atmospheres*, *123*, 8326–8343. https://doi.org/10.1029/2017JD027927

Received 24 OCT 2017
Accepted 11 JUL 2018
Accepted article online 24 JUL 2018
Published online 13 AUG 2018

Abstract Emissions of aerosols and trace gases from wildfires and their direct shortwave radiative forcing (DSRF) at the top of atmosphere were studied using satellite observations from Moderate-Resolution Imaging Spectroradiometer, Atmospheric Infrared Sounder, Clouds and Earth Radiant Energy System on Aqua, and Ozone Monitoring Instrument on Aura. The dominant fuel types of the selected fire cases in the northeast of China (NEC), Siberia (Russia), and California (USA) are cropland, mixed forest, and needle-leaf forest, respectively. For the cropland fire case in NEC, the fire radiative power-based emission coefficients (Ce) of aerosol is 20.51 ± 2.55 g/MJ, half that of the forest fire cases in Siberia (40.01 ± 9.21 g/MJ) and California (45.23 ± 8.81 g/MJ), and the carbon monoxide (CO) Ce (23.94 ± 11.83 g/MJ) was about one third and half that of the forest fire cases in Siberia and California, respectively. However, the NO_x (NO2 + NO) Ce (2.76 ± 0.25g MJ^{-1}) of the cropland fire in NEC was nearly 3 times that of those forest fire cases. Ratios of NO_x to aerosol, HCHO, and CO in the cropland case in NEC show much higher values than those in the forest fire cases. Despite the differences of the Ce and the composition ratios, the DSRF efficiency of smoke aerosol at the top of atmosphere showed similar values among those fire cases. Our results highlight the large variability of emission rate and relative chemical composition but similar DSRF efficiencies among wildfires, which would provide valuable information for understanding the impact of fire on air quality and climate.

1. Introduction

Large amounts of trace gases and aerosol particles are emitted into the troposphere during the biomass burning processes (Crutzen & Andreae, 1990; Ichoku & Ellison, 2014; Langmann et al., 2009). This emission makes great impacts on Earth climate, environment, ecosystem, and human health (Bergeron & Gauthier, 2017; Oris et al., 2013). Smoke aerosols can directly mediate the radiative energy balance in the Earth's climate by scattering and absorbing incoming solar radiation (the direct shortwave radiative forcing, hereafter DSRF), and aerosols can also indirectly modify the incoming solar radiation by affecting the microphysical properties of cloud and precipitation (Andreae et al., 2004; Christopher et al., 1996; Langmann et al., 2009; Li et al., 2010; Li & Min, 2010; Min et al., 2009, 2014; Min & Li, 2010; Patadia et al., 2008). Previous studies have pointed out that wildfires can significantly enhance the column density of nitrogen dioxide (NO_2), formaldehyde (HCHO), and carbon monoxide (CO) in the tropospheric atmosphere (Huijnen et al., 2012; Meyer-Arnek et al., 2005). Since HCHO and NO_2 are important precursors of secondary aerosol and tropospheric ozone, such enhancement may introduce large perturbations to the regional and global atmospheric composition and chemistry (Andreae & Merlet, 2001). Because the optical properties, such as absorption coefficient and single-scattering albedo of aerosol particles, highly depend on their chemical compositions, size distribution, and shapes, such perturbations may have further impacts on the DSRF. In addition, those emissions are severe threats to human health: Fine particles can be breathed into humans' lungs and have a toxic effect (Goldammer et al., 2008). NO_2 can cause inflammation of mucous membranes, and HCHO can cause changes in the mechanics of respiration and lung function.

Accurate emission information about trace gases and aerosols from fires is necessary to evaluate the biomass burning influence on the atmosphere (Langmann et al., 2009) and to improve the modeling of physical and chemical processes in wildfire. Different methods of estimating fire emissions have developed in the past three decades. However, large variations and uncertainty exist (Jaeglé et al., 2005; Kaiser et al., 2012). For example, methods based on burned area are severely constrained by the lack of information about area burned, fuel load, and the emission factor and are not suitable for estimating the instantaneous emission rate of the fire (Akagi et al., 2011; Andreae & Merlet, 2001; Ichoku & Kaufman, 2005).

Ichoku and Kaufman (2005) first developed a new method to link fire emissions of aerosols to satellite-derived fire radiative power (FRP) using observations from the Terra and Aqua satellites. Using this FRP-based method, Ichoku and Ellison (2014) obtained the gridded global aerosol emission coefficients (Ce, g/MJ) defined as mass emission of aerosol per unit energy released from fire. Mebust et al. (2011) following this method retrieved the NO_x (NO_2 + NO) Ce in California and Nevada. The mean Ce of NO_x was obtained for global biomes (Mebust & Cohen, 2014). Schreier et al. (2014) applied this method in trace gas emissions and derived NO_x Ce for selected biomes and regions.

There is also strong consistency between time series of HCHO and fire parameters such as fire count and FRP (De Smedt et al., 2015; Wooster et al., 2011). However, to our knowledge, there are very few studies on estimating FRP-based Ce values of HCHO.

As for CO, fire energy-based emission coefficients from the laboratory (Freeborn et al., 2008) and emission factors (EF expressed as g/kg; Akagi et al., 2011; Andreae & Merlet, 2001) are available, while research on FRP-based Ce using satellite data is rare.

It is not easy to derive detailed chemical composition inside the smoke. However, the ratios between different components in the smoke (e.g., NO_x to aerosol, HCHO and CO, HCHO to aerosol) can be a good indicator of its chemical composition. Veefkind et al. (2011) and Li et al. (2016) showed strong correlations of NO_x, sulfate dioxide (SO_2) to aerosol optical depth (AOD). These ratios differ remarkably among pollution sources in Asia, America, and Europe and between pollution in megacity areas and relatively rural areas in China. The differences indicate that the ratio could be used to roughly evaluate the chemical composition in the smoke and distinguish different emission sources (Li et al., 2016; Veefkind et al., 2011). In addition, the ratios of active gases to reference specie (e.g., CO) are able to reveal their relative emission amounts and represent the capability of changing the oxidation of the atmosphere to some extent.

Previous studies of emission parameters (e.g., EF and Ce) and the DSRF from smoke mainly focused on spatially and temporally averaged behavior of fire. The huge variability among individual fires has received less attention (Akagi et al., 2011; Andreae & Merlet, 2001; Mebust, 2013; Mebust & Cohen, 2014; Yokelson et al., 2003). Several factors such as vegetation type, meteorological conditions, and fuel conditions could be responsible for the variations (Ichoku & Ellison, 2014; Ichoku & Kaufman, 2005; Mebust et al., 2011; Santos et al., 2008; Schreier et al., 2014; Van Leeuwen & Van Der Werf, 2011).

Therefore, to assess the impacts of wildfire on atmospheric climate and environment, accurate estimation is needed for the fire emission parameters, the fires' chemical composition, the associated DSRF, and the fires' individual variabilities. Most importantly, it is necessary to understand the connections among these factors. Satellite remote sensing and related technology can provide critical information to do these studies. However, no single satellite system can meet all the above requirements. It is meaningful to combine observations from multiple satellites and multiple sensors to conduct an integrated analysis of the above features.

In this study, multiple fire cases were selected with representative types of fuel in the northeast of China (NEC), Siberia (in Russia), and California (in America) to conduct comprehensive investigations of the fires' impacts on atmospheric composition and DSRF. Using quasi-synchronous multiple-satellite observation, FRP-based Ce values of aerosol, NO_x, HCHO, and CO were determined. To the best of our knowledge, this study is the first to produce Ce from these four compositions simultaneously. Then we characterized the correlations among smoke aerosols, NO_x, HCHO, and CO and derived the ratios between each pair of them. Variabilities of Ce and composition ratios between individual fires were analyzed and discussed. From the understanding of the fire emissions and chemical composition, we further estimated the smoke DSRF at the top of atmosphere (TOA). These results are compared with results published in the literature, and we discuss factors, which may influence the final results.

2. Data and Methodology

2.1. Selection of Fire Cases and the Associated Dominant Fuel Type and Meteorology Conditions

Aqua MODIS detected a series of fires in East Asia in October 2004. Large areas of forest were destroyed by this series, and its widespread influence was mentioned by Goldammer et al. (2004, 2008). Among those fires, one of the largest, on 15 October 2004 in NEC, was selected as case F1. Another fire case on 30 May 2006, also in NEC, was selected as case F2. The fire series containing F2 was the most severe in the NEC area since the extreme strong fire event in 1987. The F2 series (which lasted from 21 May to 2 June 2006) is listed in the 10 most remarkable meteorological disasters in 2006 in China by the China Meteorological Bureau (http://www.gov.cn/fwxx/kp/2006-12/30/content_484190.htm).

A wave of forest fires happened in middle and late July of 2006 in Siberia, and vast areas of Russia were shrouded in thick smoke with heavy air pollution (Verma et al., 2009). The fire on 22 July 2006 captured by Aqua MODIS was selected as case F3.

Forest fires frequently occur in California. During June and July 2008, hundreds of wildfires happened and large areas of forest were burned due to record-breaking lightning activity and months of drought. Hawkins and Russell (2010) chose this series of fires as their research object. In this study, fires detected on 25 June, 9 July, and 11 July by Aqua were selected as cases F4, F5, and F6. Since the individual fire cases in California have much less satellite observation data, and the amount for the individual fires would not be enough to get a convincing result, thus, the data for F4–F6 is combined for further quantitative analysis in this work. All the selected fire/smoke cases were confirmed by the MODIS Rapid Response Project.

The dominant fuel type (Figure 1) and meteorology conditions (Table 1) associated with the fire are critical to determine the emission rate of aerosol and trace gases, and they also partially determine the strength and size of the fire. The MODIS land cover product MCD12C1 (0.05° × 0.05°; Friedl et al., 2010) with the University of Maryland classification scheme (UMD) and ERA-Interim weather data (0.125° × 0.125°) were used to provide those information. For each MODIS-detected fire pixel (1 km × 1 km), land cover type (Figure 1) and meteorological parameters (Table 1) from the nearest grid of MCD12C1 and ERA-Interim are assigned. The ERA-Interim reanalysis data set is produced by European Centre for Medium-Range Weather Forecasts (ECMWF). To generate such data set, a four-dimensional variational analysis approach is used to assimilate various input products including in situ measurements from satellite and conventional observations. In this study, the major data used are wind vectors at 850 hPa as suggested by Ichoku and Kaufman (2005) and Ichoku and Ellison (2014) for that most smoke plumes height are about 1.5 km ± 1 km (Ichoku & Ellison, 2014).

The major uncertainties involved in the parameters listed in Table 1 come from two sources. One is the original uncertainty of the ERA-Interim reanalysis data set. The detailed discussion of the data quality of ERA-Interim reanalysis data can be found in Dee et al. (2011). This measurement error is not reflected in the results. The other uncertainty is from the areal variability. We calculated the mean value and the standard deviation from all fire pixels for each fire case. For example, the averaged wind speed at 10-m height for case F1 is 7.63 m/s, and the associated standard deviation due to areal variability is 1.01 m/s.

The fuel composition of fire cases was shown in Figure 1. For the F1 case in NEC, 44.7% of burned vegetation was cropland, followed by woody savannas 28.3%, grassland 12.9%, and a small percentage of forest. Most of the burned fuels were relatively fine stems and branches. For the other cases, the dominant fuel type was forest, and the percentages were 53.4% (50.7% mixed forest) for the F2 case, 66.4% (36.0% mixed forest) for the F3 case, and 80.6% evergreen needle-leaf forest for the F4–F6 cases. Generally, forest fuel types have bigger stems and branches than cropland, savannas, and grassland.

Weather conditions were also very different among those fire cases (see Table 1). The near-surface (10-m altitude) wind speed was the highest (7.63 ± 1.01 m/s) in F1, which was 1.75–2.0 times the values in other cases. The temperature was highest in the F4–F6 cases and lowest in F1. The differences between temperature and dew point temperature were about 20 and 30 K in cases F2 and F4–F6, indicating that the relative humidity was the lowest in those cases.

In brief, F1 was a cropland dominant case, featuring relatively high near-surface wind speed. F2 and F3 were mixed forest dominant cases, and F4–F6 were evergreen needle-leaf forest dominant cases. Moreover, cases F2 and F4–F6 occurred in relatively dry atmospheres. In all cases, there were considerable areas of woody savanna and savanna.

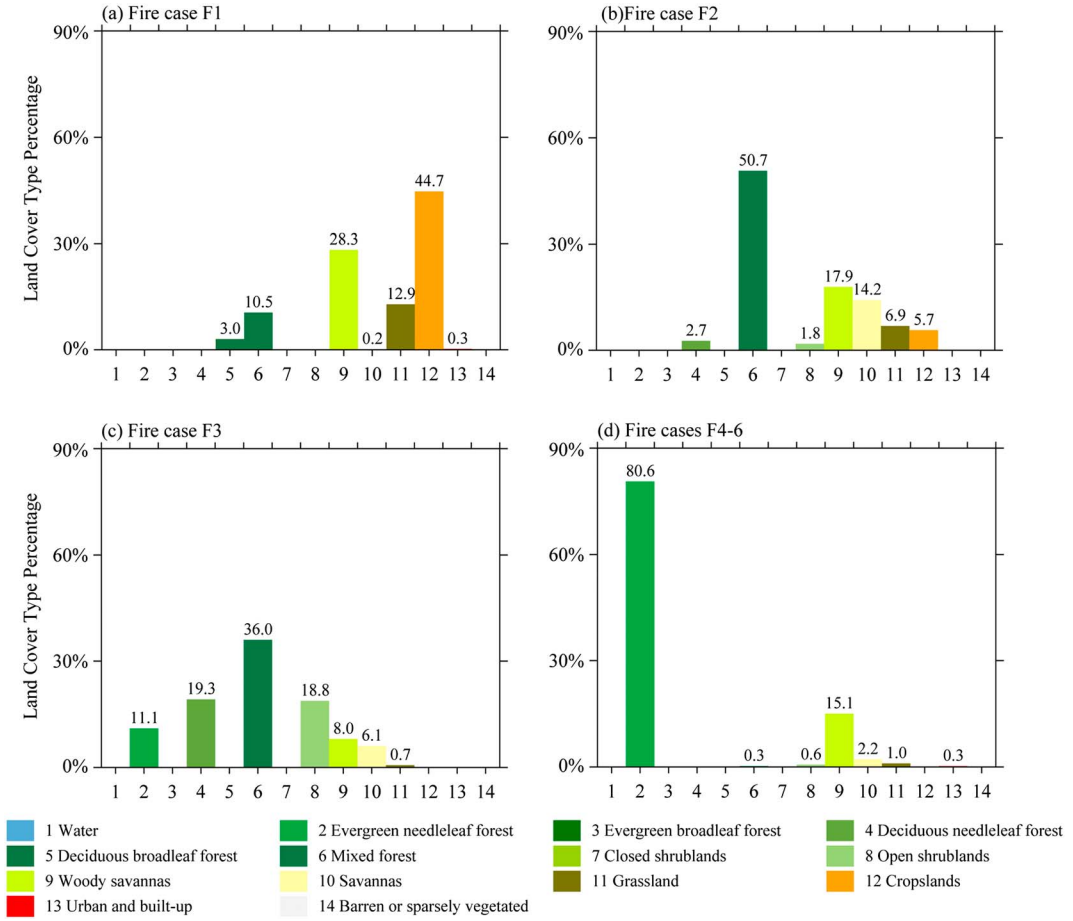

Figure 1. The land cover percentage (%) for (a) fire case F1 in the northeast of China, (b) fire case F2 in the northeast of China, (c) fire case F3 in Siberia, Russia, and (d) fire cases F4–F6 in California, USA. Based on MODIS land cover product MCD12C1.

2.2. Satellite Observations of Fire, Aerosols, Trace Gas, and Upwelling Radiation Flux

The A-train satellite constellation can provide quasi-synchronous observations of fire, aerosols, and trace gases. It provides researchers with a unique opportunity to study the intensity and size of a fire, the fire emissions, and the relationships among different compositions in the smoke. The multiple-platform and multiple-sensor satellite observation products and ancillary atmosphere reanalysis data set utilized in this study are listed in Table 2.

Aqua MODIS identifies hot spots by applying the contextual algorithm (Giglio et al., 2003), which is based on the contrasts of brightness temperature at 4 and 11 μm between fire and nonfire pixels. The validation and

Table 1
Basic Information of Selected Fire Cases

	F1	F2	F3	F 4–F6
Fire cases (MODIS fire pixels)	2,385	1,089	1,194	782
Geographic region	Northeastern China	Northeastern China	Siberia	California
Geo-location	40–55°N, 120–145°E	48–57°N, 120–135°E	50–70°N, 75–115°E	35–45°N, 110–125°W
Detection time (UTC)	15 October 2004	30 May 2006	22 July 2006	25 June, 9 July, and 11 July of 2008
Dominant fuel type	Cropland	Mixed forest	Mixed forest	Evergreen needle-leaf forest
10-m wind speed (m/s)	7.63 ± 1.01	4.00 ± 1.41	4.35 ± 1.57	3.69 ± 1.08
2-m dew point temperature (K)	262.97 ± 4.68	281.74 ± 2.00	284.08 ± 2.09	277.89 ± 5.42
2-m mean temperature (K)	282.10 ± 4.47	301.02 ± 2.11	298.98 ± 1.27	307.16 ± 5.50

Table 2
Satellite Products and Reanalysis Data Sets Used in This Study

Main parameters (unit)	Data products	Sensors	Level	Resolution
Reflectance	MYD02HKM	Aqua MODIS	L1	500 m*500 m
Fire Radiation Power (MW)	MYD14		L2	1 km*1 km
AAOD	OMAERUV	Aura OMI	L2	13 km*24 km
NO_2 (molecules/cm^2)	OMNO2			
HCHO (molecules/cm^2)	OMHCHO			
Total column CO (molecules/cm^2)	AIRX2RET	Aqua AIRS	L2	41 km*41 km
Shortwave Radiation Flux (MW/m^2)	SSF	Aqua CERES	L2	20 km
Weather data	ERA Interim	ECMWF	~	0.125°*0.125°

accuracy of Aqua MODIS fire detection have been examined by Hawbaker et al. (2008) with detection rate of 73%. FRP was estimated for each fire pixel using the empirical method of Kaufman et al. (1998) with minimum detectable fire of 10–20 MW. In this study, the latest fire product MYD14 version 6 (Giglio & Justice, 2015) with the pixel size of 1 km × 1 km is used.

Aura Ozone Monitoring Instrument (OMI) is an ultraviolet/visible (UV/VIS) nadir solar backscatter spectrometer. It provides measurements of aerosol optical depth and column density of ozone and trace gases with nominal resolution of 13 km × 24 km.

In product of OMAERUV (Torres, 2006), the aerosol absorption optical depth (AAOD) was retrieved at the near-ultraviolet spectrum, which is very sensitive to smoke-absorbing aerosol with root-mean-square error ~0.01. The aerosol optical depth (AOD) has been proved to be reliable under the cloud-free condition, and the retrieval mean square error over land is expected to be about 0.1 or 30%, whichever is larger (OMI Team, 2012).

In product of OMNO2 (Krotkov & Veefkind, 2016), the tropospheric column mole density of NO_2 was retrieved at the OMI visible spectrum ranging from 405 to 465 nm, using the differential optical absorption spectroscopy method. As a reference, the noise of NO_2 tropospheric column density is about $0.45 \pm 0.04 \times 10^{15}$ molecule/cm^2 over the tropical South Pacific region (Krotkov et al., 2017).

In product of OMHCHO (Kelly, 2007), the vertical column density of HCHO is retrieved from the OMI spectrum of 306–364 nm and the typical uncertainties range from 50% to 105% (OMI Team, 2012).

The total column density of CO (molecules/cm^2) was provided by the Aqua Atmospheric Infrared Sounder (AIRS) level 2 product AIRX2RET (AIRS Science Team/Joao Texeira, 2013). It has been validated by McMillan et al. (2011), and the accuracy of observation is typically 10%.

In addition, the upwelling shortwave radiation flux (0.3–5 μm, W/m^2) at the top of atmosphere (TOA) estimated from the Clouds and the Earth Radiant Energy System (CERES) on Aqua satellite (Patadia et al., 2008; Wielicki et al., 1996) was used to estimate the shortwave (SW) radiative forcing effect of smoke aerosol (showed in Figure 8). The overall bias of CERES estimation is less than 0.2 W/m^2, and the root-mean-square errors range from 0.70 to 1.4 W/m^2 (Loeb et al., 2007).

The reflectance products from MODIS MYD02HKM are used for RGB (red, green, blue) images composition (Figures 2a–2c).

2.3. Calculation of Mass Emission Rate of Aerosol and Trace Gases

The basic concept and method used here was first developed by Ichoku and Kaufman (2005) for aerosols Ce estimation. Mebust et al. (2011) and Schreier et al. (2014) applied it to trace gas NO_2. We followed those methods and applied it to estimate Ce of aerosol and more trace gases including NO_2, HCHO, and CO. The method and its major assumptions are introduced here briefly.

Satellite observations of aerosol optical depth or column concentration of trace gases are the results of cumulated emissions over a finite period of time in the pixel area. Therefore, the mass emission rate (g/s^1) can be obtained by dividing the total emitted mass of aerosol and those trace gases (g) by the accumulative time (s). For certain pollutant, the total emitted mass from fire can be estimated by timing the mass area density of M_f (g/cm^2 or g/m^2) with the area of the satellite observing pixel A_{pixel} (m^2). The accumulative time T_{pixel} can be determined by the A_{pixel} and the mean wind speed at the smoke injection height.

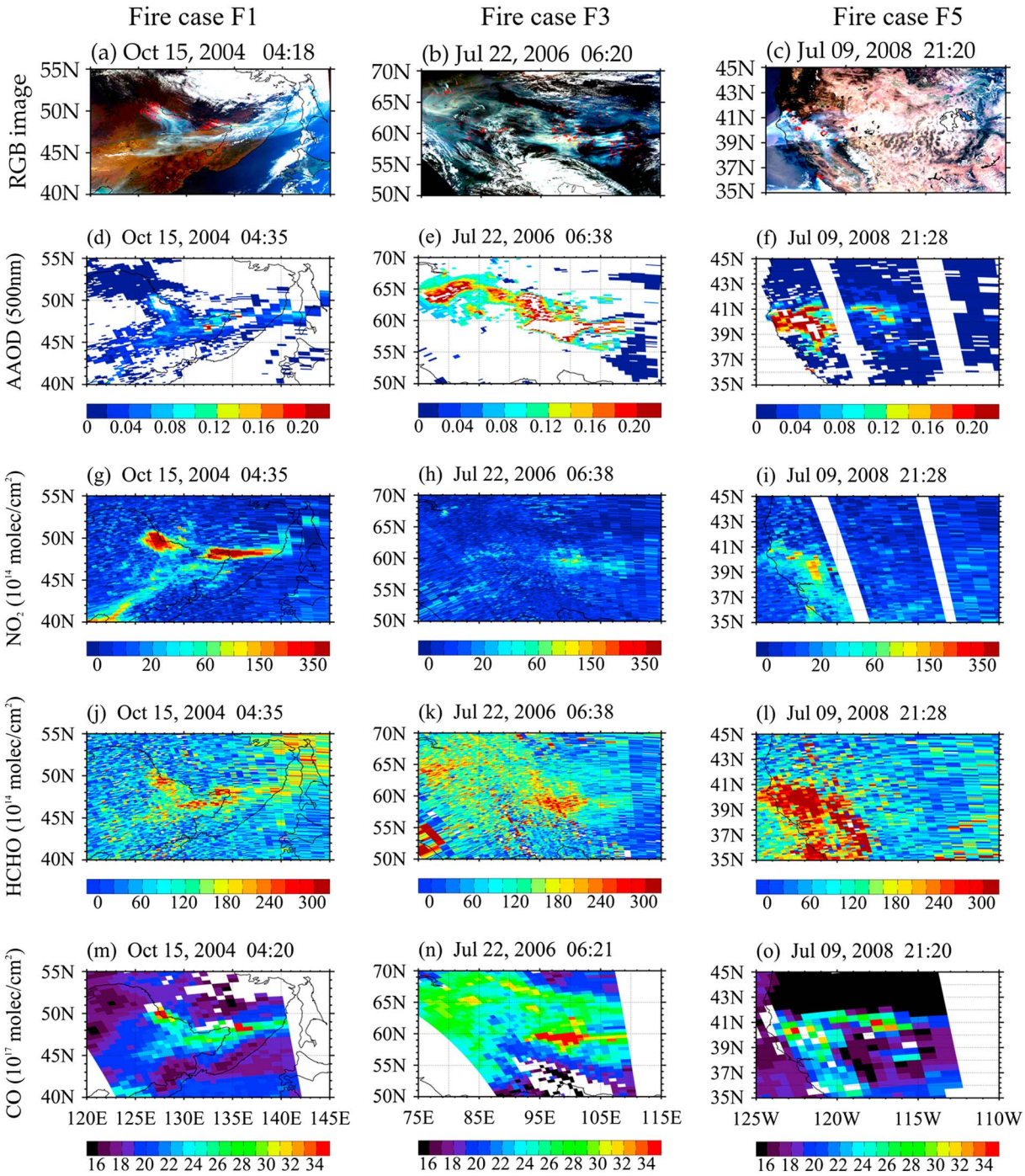

Figure 2. From left to right: selected fire cases F1, F3, and F5. From top to bottom: the RGB composite true color images from MODIS, AAOD, tropospheric vertical columns density of NO_2, vertical column density distribution of HCHO from OMI retrievals, and total column density distribution of CO from AIRS retrievals. All observations are shown in UTC time.

First, the satellite-observed aerosol optical depth or column molar density (molecule/cm^2) needs to be converted to mass area density.

$$M_f = (\mathrm{Pa}_{\max} - \mathrm{Pa}_{\min}) * k \quad (1)$$

where $\mathrm{Pa}_{\max}$ and $\mathrm{Pa}_{\min}$ is the maximum and minimum satellite observations of pollutants among the considered satellite pixel and its surrounding eight pixels (for aerosol) or its three downwind pixels (for

NO_2, HCHO, and CO), respectively. Parameter k stands for mass conversion coefficient, which is different for each pollutant.

For aerosol, $k = 1/\beta$, where β (m^2/g^1) is the aerosol mass absorption efficiency. Based on the work of Reid et al. (2005), the value $\beta = 0.4 m^2/g^1$ for smoke of temperate/boreal forest fires was used in the current work because all of the fire cases occurred in the temperate/boreal forest region.

For NO_2, $k = [MM * (1 + NO/NO_2)]/N_A$, where MM (g/mol) is the molar mass of NO and Avogadro's constant is $N_A = 6.022 \times 10^{23}$ (molecules/mol). The term $1 + NO/NO_2$ (without unit) is the inverse of $NO_2/NOx(NO_x = NO + NO_2)$. The ratio of NO_2/NO_x is set as 0.75 as suggested by Mebust et al. (2011) and Schreier et al. (2014).

For HCHO and CO, $k = MM/N_A$, where MM (g/mol) is the associated molar mass of HCHO and CO.

Second, the cumulative time T_{pixel} (in seconds) of the aerosol and trace gases in the satellite pixel is estimated by

$$T_{pixel} = \sqrt{A_{pixel}} / \sqrt{u_{pixel}^2 + v_{pixel}^2} \quad (2)$$

where u_{pixel} and v_{pixel} are the zonal and meridional wind speed (m/s) at 850 hpa (for cases F1, F2, and F3) and 800 hpa (for cases F4, F5, and F6) derived from ERA-Interim reanalysis data. Although the smoke injection height varied from case to case, globally, most fires inject smoke to height less than 3.0 km. The global average injection height of 1.5 km (around 850 hpa) therefore was suggested by Ichoku and Kaufman (2005). Sensitive tests of wind speed for all study cases were conducted by comparing the results of using the wind speed at 900 hPa level, and it was found that most of the Ce change only less than 10% (refer to the supporting information).

Finally, the mass emission rates R_{pixel} (in g/s) were obtained by dividing the total mass of emission by the accumulative time:

$$R_{pixel} = M_f * A_{pixel} / T_{pixel} \quad (3)$$

The setting of aerosol absorption coefficient β as 0.4 m^2/g, the setting of the ratio of NO_2/NO_x as 0.75, and the selection of 850 and 800 hpa as the averaged smoke injection layer are the three major assumptions in this method.

It should be noted that the original spatial resolutions of satellite observations were about 13 km × 24 km for aerosol, NO_2, and HCHO and 41 km × 41 km for CO. However, in the study of FRP-based emission efficiency Ce (section 3.2), the spatial resolution was adjusted to 1° × 1° resolution. This was done by collocating all satellite pixels into their associated 1° × 1° grid and summing up the FRP and fire emission rates R_{pixel} in it to represent the total FRP and Ce of the grid. This is helpful to reduce the spatial variability based on the works by Ichoku and Ellison (2014) and Schreier et al. (2014).

3. Results

This section provides summary of the results for the studied six fire cases. The discussion and explanation of the differences among cases are presented in section 4.2.

3.1. Spatial Distributions of Fire, Aerosol, and Trace Gases

RGB composite true color images of fire cases F1, F3, and F5 (F2, F4, F6, and map of dominant vegetation type are shown in the supporting information) occurring in China, Russia, and California are shown in Figure 2. The number of fire points (red dots) in the cropland fire F1 is 2,385, which is twice that in the mixed forest case F3 (1,194) and about 7 times that in the needle-leaf forest case F5 (371). The number of fire points indicates the size of the fire and that F1 is the largest. In addition, those fire points in the cropland fire F1 are denser than other cases and this indicates that the FRP of F1 is the greatest as well. Over the fire points and in their downwind area, the smoke is in gray and blue colors. In the contiguous areas, higher values of AAOD, NO_2, HCHO, and CO are presented. Generally, there are good spatial correlations among them. The source of atmospheric aerosol is complicated. For example, in the studying area in Northeastern China, the AOD can be significantly

affected by mineral dust from the upstream Gobi and Taklimakan desert (Li et al., 2017; Wang, Liu, et al., 2018; Wang, Wen, et al., 2018), and in that case, AOD has no correlations with trace gases. Therefore, the good correlation shown in Figure 2 indicated that those pollutants were mainly emitted from the fire and transported downwind. On the other hand, because those satellite retrievals were made from different algorithms independently, the results also indirectly proved their validity.

Remarkable differences of fire emissions among those cases are seen in Figure 2. Considering aerosols, AAOD is the lowest in the cropland case F1 compared to the forest cases of F3 and F5, regardless of the fact that the size and intensity of the fire is greatest in F1. Meanwhile, it is noteworthy that the column density of NO_2 in F1 is much larger than those in the other cases.

The HCHO spread to a larger area in F3 compared to others, but the accumulated concentration of HCHO is the highest in F5. For CO, the regional difference is relatively smaller than for the other three trace gases.

The associated mass emission rate combining both satellite retrievals and horizontal wind field information is shown in Figure 3. Generally, the spatial pattern of mass emission rate of each component is similar to satellite observations shown in Figure 2. However, differences between satellite-observed concentration (or optical depth) of pollutants and the mass emission rate (g/s) can be seen in some areas. For example, in the fire pixels in Figure 2n around 65°N and 105°E, the satellite-observed column density of CO is high; however, the mass emission rate of CO from this area in Figure 3k actually is very low due to the slow wind speed and thus has long accumulative time T_{pixel} there. This proved the advantages of converting the direct satellite observations of pollutants to associated mass emission rate using the method described in section 2.3.

3.2. The Relationships Between Fire Emissions and FRP

In Ichoku and Kaufman (2005), it was pointed out that the FRP can represent the combined information of the burned area, the biomass density, the fraction of above-ground biomass, and the burn efficiency. This means that FRP is a good proxy parameter to estimate the fire emission rate at an instantaneous time.

As shown in Figure 4, the emission rates of aerosol, NO_x, HCHO, and CO using a 1° × 1° grid cell showed the consistent trend of increasing with FRP. Generally, the emission of all pollutants increases with increasing FRP. For given FRP, the emission rate shows considerable scattering, particularly at low FRP ranges. Such scattering represents the spatial variability in the FRP-Ce relationships. One possible reason of such variability is due to fuel type. And the other possible reason is due to the stages of combustion at different places when satellite overpassing. From the plot, in each case, when FRP is low, the spatial variability of fire emission rate is large (Figures 4b, 4c, and 4l), but when FRP gets larger, the positive correlation between them becomes stronger and the spatial variability of fire emission rate becomes relatively small. Therefore, it is expected that the uncertainty of fire emission rate is large for small FRP than that for large FRP. A statistical study for deriving the FRP-fire emission rate relationship at classified spatial locations, fuel type, and combustion stages using more samples is undergoing. The spatial variability will be taken better care of in that study.

The correlation between the emissions and the FRP all passed the 95% confidence level of the Student's *T* test (except for Figure 4p, which may be due to the small grid samples). Here are some findings from this study that help to characterize this correlation: (1) The correlation is stronger when FRP is larger. This is particularly clear in case F3 (most samples have FRP less than 2,000 MJ/s). Actually, in each case, when FRP is small, the dependence of emission rate on FRP is more scattered, but when FRP gets larger, the positive correlation between them becomes stronger. (2) Comparing the correlation between FRP and different pollutants, the NO_x-FRP correlation is the strongest (R = 0.64–0.84), followed by the aerosol-FRP correlation (R = 0.45–0.83).

In addition, it is worth to note that the CO-FRP correlation (0.26) in the cropland case F1 is much weaker than those found in the other cases (R = 0.44–0.53). This is due to some samples that showing very high emission rates of CO of 750 kg/s with very weak FRP of ~1,000 MW.

The FRP-based emission coefficients Ce, defined as the linear regression slope between mass emissions rate against FRP, are summarized in Figure 5. Significant differences were found among cases.

In the cropland fire case F1 in NEC, the FRP is the strongest among all the cases but the estimated Ce value of smoke aerosol is only 20.51 ± 2.55 g/MJ, which is half of that in Siberia (40.01 ± 9.21 g/MJ) and in California (45.23 ± 8.81 g/MJ).

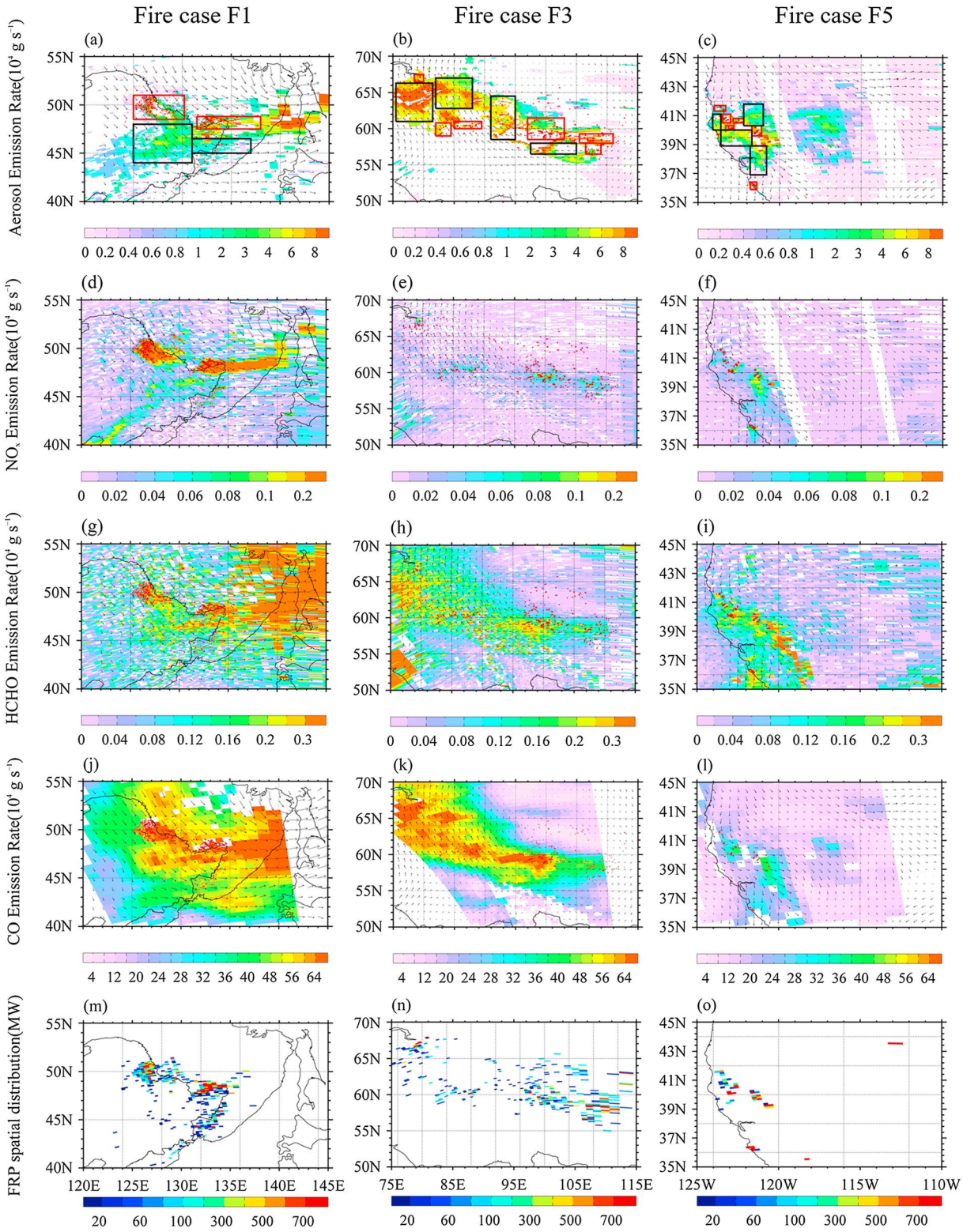

Figure 3. From left to right: selected fire cases F1, F3, and F5. From top to bottom: spatial distributions of mass emission rates (g/s) of aerosol, NO_x, HCHO, CO, and FRP (MW). Overlapping arrows are horizontal wind vectors derived from ERA-Interim. Red dots indicate fire points, and the red and black boxes define samples near or distant from fires.

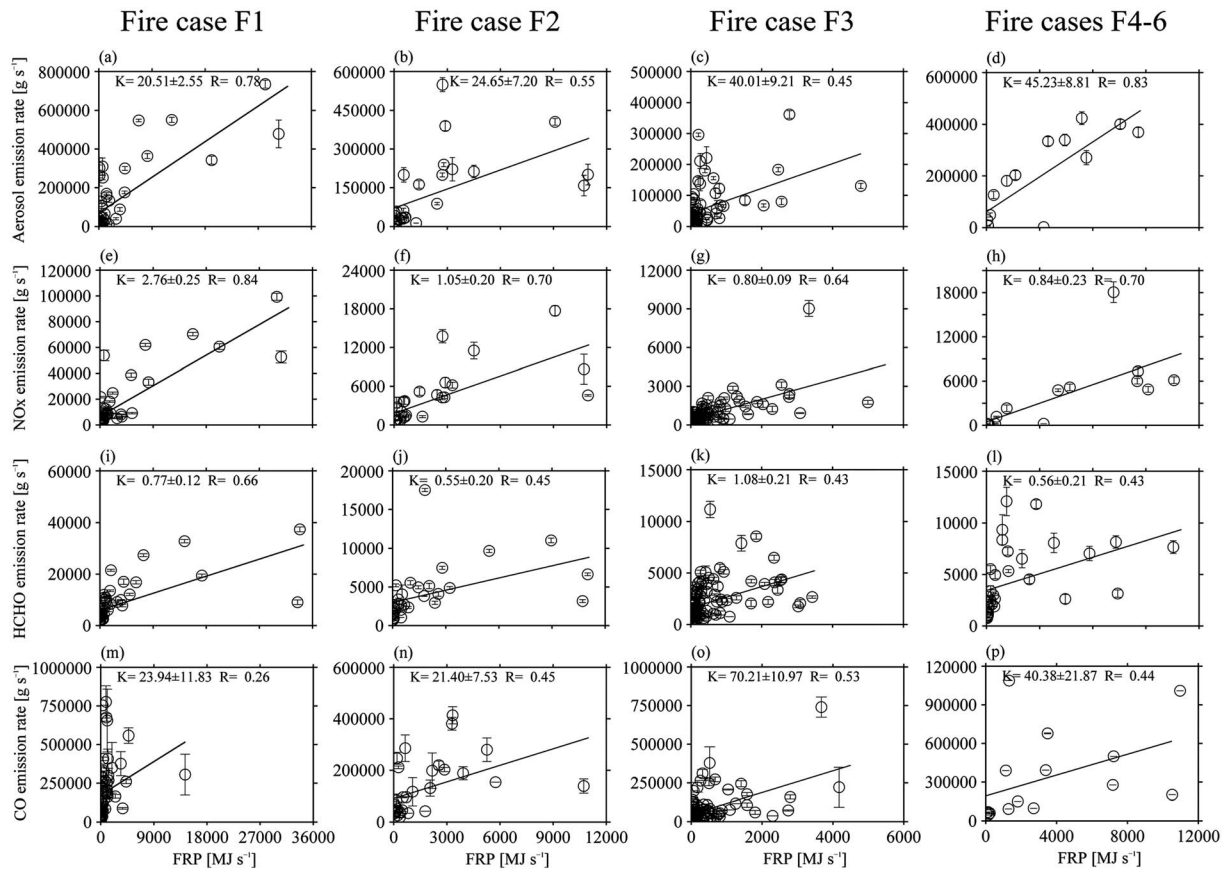

Figure 4. Scatterplots of (a–d) aerosol emission rates against FRP, (e–h) NO_x emission rates against FRP, (i–l) HCHO emission rates against FRP, and (m–o) CO emission rates against FRP for fire cases F1, F2, F3, and F4–F6, respectively. Open circles represent one 1° × 1° grid data sample, and vertical error bars are emission standard errors of each 1° × 1° grid cell. K is the fitting slope (g/MJ) and its 1-sigma uncertainty estimates, and *R* is the correlation coefficient.

Contrary to the aerosol emission observations, the highest NO_x Ce value (2.76 ± 0.25 g/MJ) is found in the cropland fire in NEC, while much lower Ce values are observed in Siberia (0.80 ± 0.09 g/MJ) and California (0.84 ± 0.23 g/MJ; see Figures 3e–3h).

No significant difference of HCHO emissions exists in the fire cases, since the Ce values of F1, F2, F3, and F4–F6 are 0.77 ± 0.12 g/MJ, 0.55 ± 0.20 g/MJ, 1.08 ± 0.21 g/MJ, and 0.56 ± 0.21 g/MJ, respectively.

The lowest Ce of CO values (23.94 ± 11.83 g/MJ and 21.40 ± 7.53 g/MJ) appeared in the cases of F1 and F2 in NEC, while much higher Ce values of 70.21 ± 11.00 g/MJ and 40.38 ± 21.87 g/MJ appeared in Siberia and California, respectively. Detailed information was summarized in Table 3.

3.3. The Relationships Among Multiple Components in Smoke

The quantitative relationships among different smoke compositions can carry important information about the emission source and the combustion process. For example, Veefkind et al. (2011) indicated that the AOD to NO_2 ratios of biomass burning are about 2 orders of magnitude higher than that over industrialized region; Yokelson et al. (2003) used the excess mixing ratios between CO and CO_2 to estimate the relative amount of flaming and smoldering combustion of fires. CO as an important emission composition from biomass burning is generally used as the reference gas for estimating the emission of other trace gases. Here we explored the relationship between CO and other three compositions.

As shown in Figure 6, strong positive correlations between the R_{sa}, R_{NOx}, R_{HCHO} versus R_{CO} were found. All correlations are statistically significant based on the Student's *T* test (95% confidence level). Among them, the correlation between R_{HCHO} and R_{CO} is the strongest.

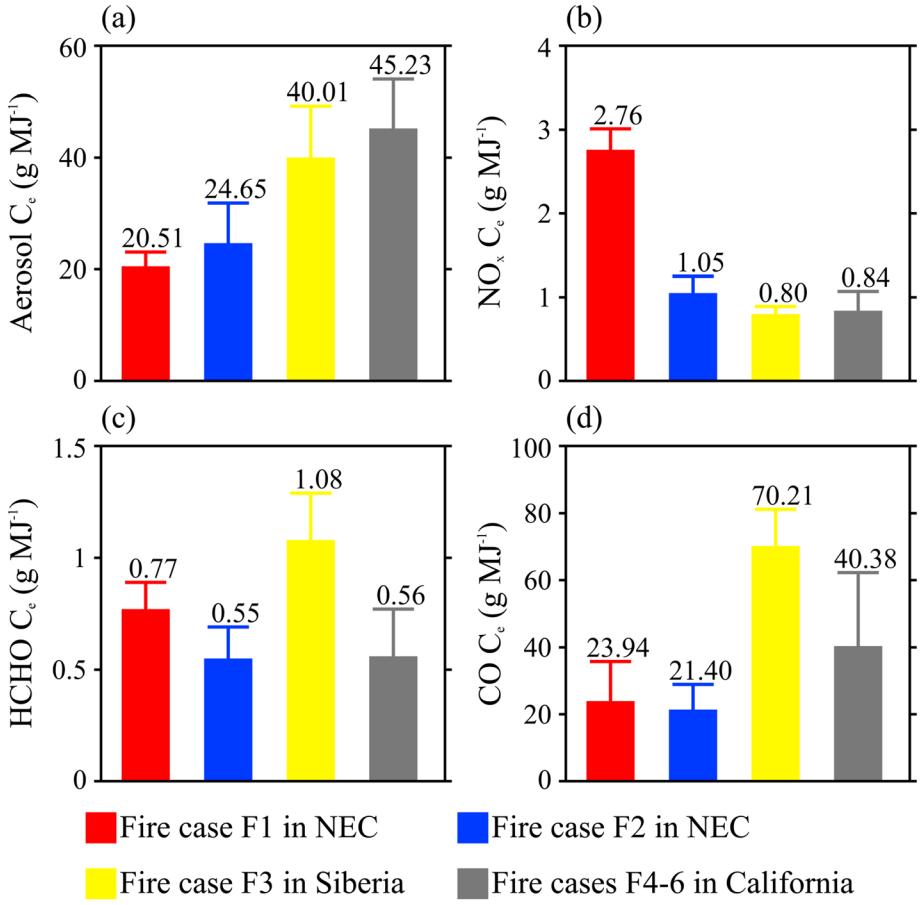

Figure 5. Histograms of Ce (in g/MJ) of (a) smoke aerosol, (b) NO_x, (c) HCHO, and (d) CO for fire cases F1, F2, F3, and F4–F6. The error bars are 1-sigma uncertainty estimates of Ce.

The ratios of R_{sa} to R_{CO} ranged from 0.078 to 0.147 among those fires, and the ratios of HCHO to CO (0.002–0.003) presented no significant differences among cases. However, the ratios of NO_x to CO show huge discrepancies, with the highest value of 0.005 in the cropland case F1 in NEC is about 25 (10) times that of the forest cases in Siberia (California).

Other relationships between different components in the smoke are shown in Figure 7, in which we separate the samples into two groups: the group near the fire source (NS) indicated by the red rectangles in Figure 3 and the group distant from the fire source (DS) indicated by the black rectangles in Figure 3.

The ratios of NO_x to smoke aerosols (R_{NOx} to R_{sa}) are much larger in the near-fire source regions than in the far fire source regions in cases F1, F2, and F3 (Figures 7a–7c), and similar results are also seen in the ratios of NO_x to HCHO (Figures 7i–7k). However, the ratios of HCHO to aerosol (R_{HCHO} to R_{sa}) showed no noteworthy difference between the two kinds of regions (Figures 7e–7g). The above characteristics did not appear in the California cases (Figures 7d, 7h, and 7l). This is most likely due to the smoke regions in California being too small to clearly distinguish the near-fire source and far fire source areas.

It should be notified that we simply separate the NS and DS visually based on the satellite image. Instead of making a quantitative comparison between NS and DS, only qualitative discussions are made to help understanding the lifetime effect of trace gas on observation.

Regional differences are another noteworthy characteristic. The slopes of the scatterplots between R_{sa} and R_{NOx} are 0.105 and 0.031 for F1 and F2 in the NEC, and these are much higher than in the Siberia and California cases (Figures 7a–7d). Similar results are revealed between R_{NOx} and R_{HCHO} (Figures 7i–7l). Discussion and explanation of those differences are given in section 4.

Table 3
FRP-Based Emission Coefficients (Ce) Derived From This Study and Results in Literature

	Fire case	Ce [g MJ^{-1}]	R	r_c	1-sigma	Referenced Ce [g MJ^{-1}]
R_{sa}- FRP	F1	20.51	0.78	0.29	2.55	6.28–50.80 [a]
	F2	24.65	0.55	0.37	7.20	7.34–37.50 [a]
	F3	40.01	0.45	0.23	9.21	1.63–109.00 [a]
	F4-F6	45.23	0.83	0.53	8.81	20.5–37.90 [a]
R_{NOx}-FRP	F1	2.76	0.84	0.27	0.25	0.24 ± 0.07–0.61 ± 0.08 [b]
	F2	1.05	0.70	0.34	0.20	0.25 ± 0.03–0.36 ± 0.02 [b]
	F3	0.80	0.64	0.18	0.09	0.28 to 1.56 [b]
	F4-F6	0.84	0.70	0.50	0.23	
R_{HCHO}-FRP	F1	0.77	0.66	0.27	0.12	0.11–1.07 [c]
	F2	0.55	0.45	0.35	0.20	
	F3	1.08	0.43	0.18	0.21	
	F4-F6	0.56	0.43	0.34	0.21	
R_{CO}-FRP	F1	23.94	0.26	0.25	11.83	32.88 and 45.58 [b]
	F2	21.40	0.45	0.34	7.53	26.65 ± 8.2–43.87 ± 15.17 [c]
	F3	70.21	0.53	0.19	10.97	
	F4-F6	40.38	0.44	0.50	21.87	

Note. R presents the Pearson correlation coefficient, r_c presents the critical correlation coefficient, and sigma is 1-sigma uncertainty estimates.
[a]Ce extracted from Ichoku and Ellison (2014) over the near-source areas. [b]Ce collected from Mebust et al. (2011), Mebust and Cohen (2014), Schreier et al. (2014), and Freeborn et al. (2008). [c]Ce converted from EF (g/kg) with the EMC of 0.41 kg/MJ.

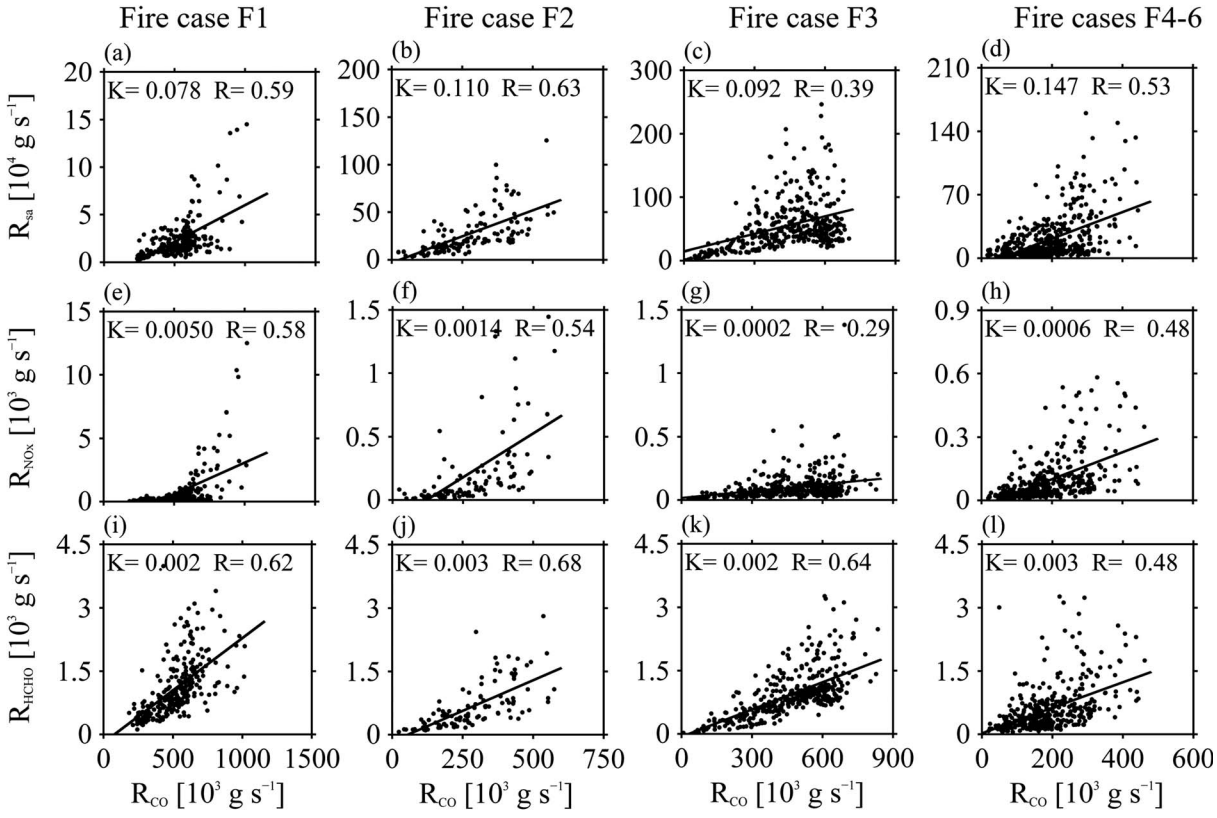

Figure 6. Scatterplots of (a–d) aerosol against CO emission rates, (e–h) NO_x against CO emission rates, and (i–l) HCHO against CO emission rates for fire cases F1, F2, F3, and F4–F6.

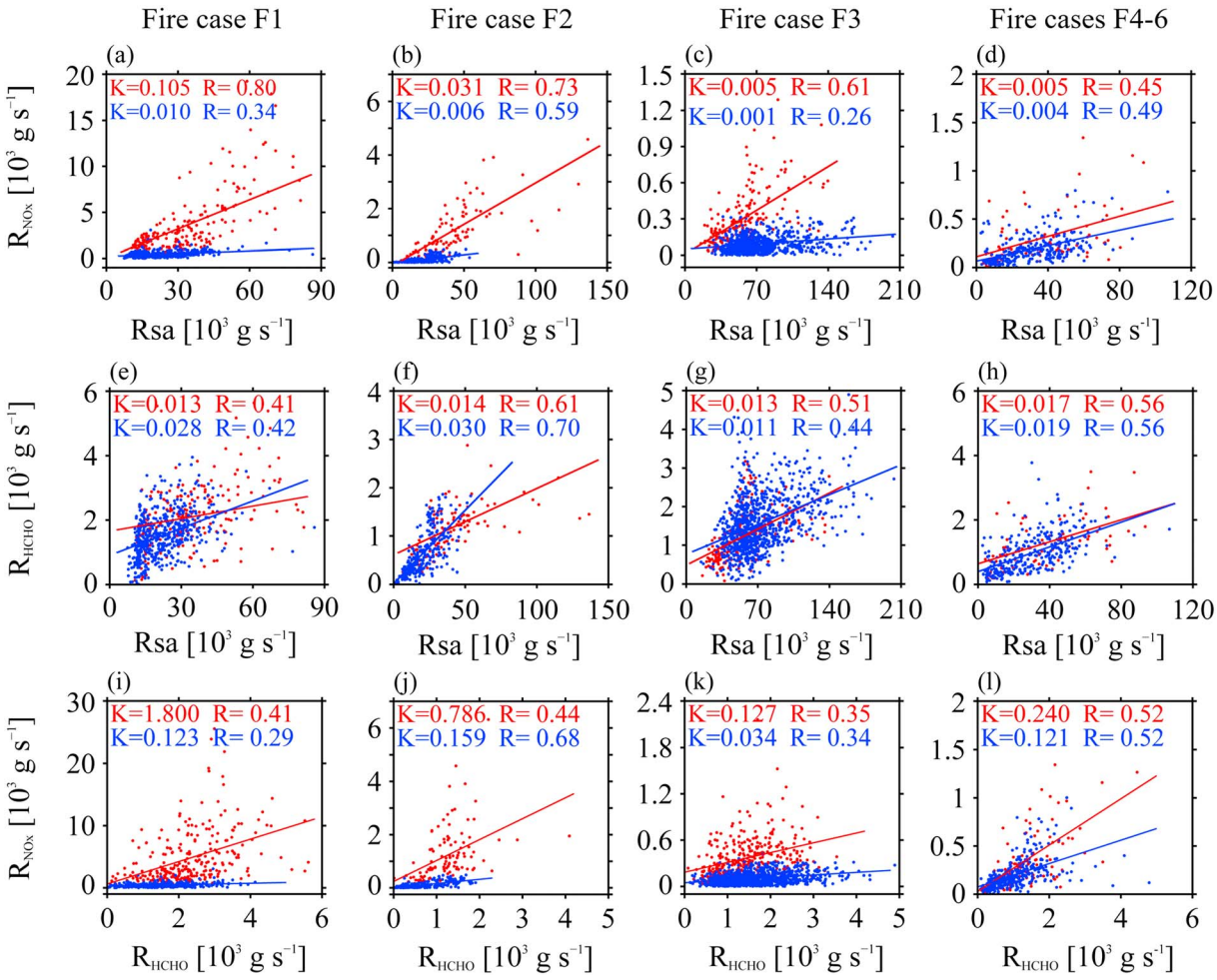

Figure 7. Scatterplots of (a–d) NO_x against smoke aerosol emission rates, (e–h) HCHO against smoke aerosol emission rates, and (i–l) NO_x against HCHO emission rates for cases F1, F2, F3, and F4–F6. Red (blue) lines and red (blue) dots represent samples near (distant from) the fire source.

3.4. Direct Shortwave Radiative Forcing (DSRF) at the Top of Atmosphere

Previous study (Patadia et al., 2008) showed that the CERES shortwave (SW) fluxes in pixel level detected by SW channel can be used to assess the DSRF effect of smoke. In this sector, the nearly coincident satellite observations of upwelling SW fluxes (W/m^2) at TOA from Aqua CERES SSF and aerosol optical depth (AOD) at 500 nm from Aura OMI were combined together to explore the smoke aerosol SW radiative forcing effect.

Figures 8a–8d show the spatial distributions of upwelling SW radiation flux at TOA in cases of F1, F2, F3, and F5, respectively (F4 and F6 are not shown here). As the figure shows, the upwelling SW flux at the TOA over smoke regions is significantly larger than that over clear sky, indicating the strong SW radiation forcing from smoke aerosols.

The direct shortwave radiative forcing (DSRF) is defined as

$$\mathrm{DSRF} = [\mathrm{SW\ Flux}]_{\mathrm{smoke}} - [\mathrm{SW\ Flux}]_{\mathrm{b}} \tag{4}$$

The $[\mathrm{SW\ Flux}]_{\mathrm{smoke}}$ stands for upwelling SW radiation flux at the TOA (in $W\ m^2$) from the smoke area. The $[\mathrm{SW\ Flux}]_{\mathrm{b}}$ presents the background upwelling SW flux at TOA over the clear-sky area (in W/m^2), which is defined as the minimum SW radiation flux value extracted from 100% clear-sky CERES footprints in the selected studying area (i.e., the red dots in Figures 8a–8d).

Strong linear correlations between DSRF and AOD (500 nm) are presented in all cases. Instantaneous DSRF coefficients of F1, F2, F3, and F4–F6, respectively, are 20.09 $Wm^{-2}\tau^{-1}$ (τ represents AOD at 500 nm),

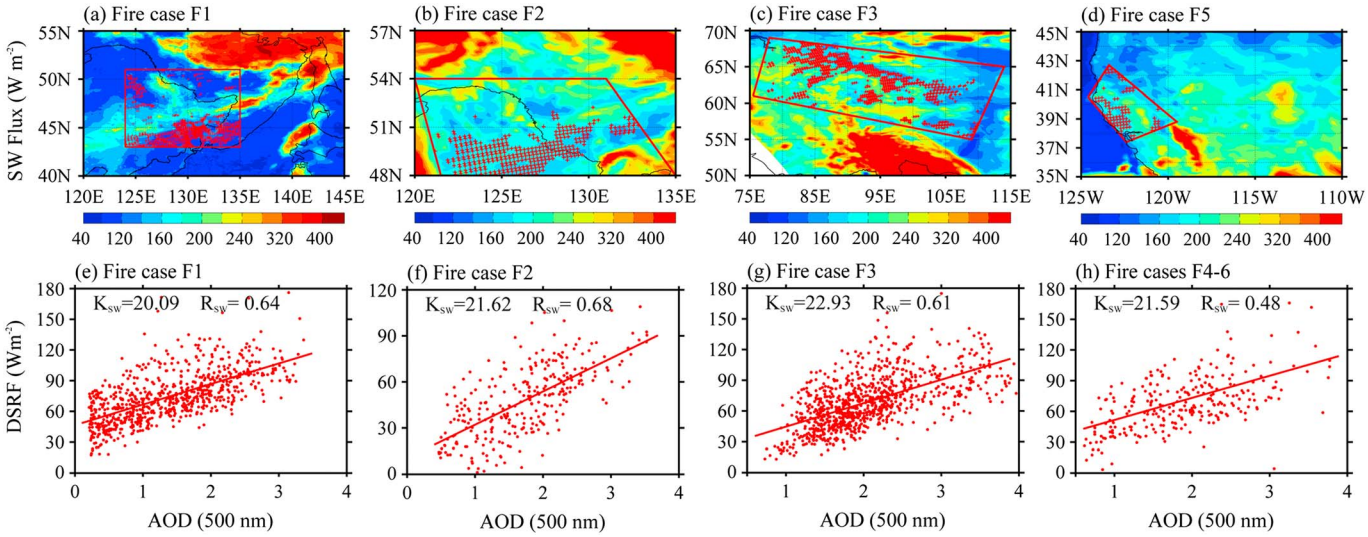

Figure 8. (a–d) Upwelling shortwave radiation flux (SW) at TOA measured by Aqua CERES for fire cases F1, F2, F3, and F5. Red boxes are the selected study areas for bottom scatterplots, and red dots are the 100% clear-sky CERES pixels. (e–h) Scatterplots of shortwave radiative forcing at the TOA versus aerosol optical depth (AOD). The K_{SW} is fitting slope, R_{SW} is 1-sigma uncertainty of the fitting slope.

21.62 $Wm^{-2}\tau^{-1}$, 22.93 $Wm^{-2}\tau^{-1}$, and 21.59 $Wm^{-2}\tau^{-1}$, showing good consistencies among each other. The 1-sigma uncertaintyof estimations of DSRF efficiency is 1.40 $Wm^{-2}\tau^{-1}$for fire cases F1 and F2 in the Northeastern of China, 1.01 $Wm^{-2}\tau^{-1}$ for fire case in Siberia, and 2.41 $Wm^{-2}\tau^{-1}$ for fire cases in California.

4. Discussion

The above results all came from case studies, so evaluation of the reliability of those results is necessary. In this section, we compare our results with previous works and attempt to explain the remarkable differences of fire emissions and composition ratios among cases.

4.1. Comparison of Ce With Results in Literature

For FRP-based Ce of aerosol, Ichoku and Kaufman (2005) yielded Ce values in a range 20–100 g/MJ, which is similar to our values (20.5–45.23 g/MJ). They also obtained the Ce values of 48 g/MJ (Terra) and 66 g/MJ (Aqua) in the Siberia region, which is slightly higher than the current Siberia fire case (40.01 g/MJ). Moreover, Ichoku and Ellison (2014) developed the global aerosol Ce data set in 1° × 1° grids with the Ce ranges from 0 to 477 g/MJ and most of those data points were less than 100 g/MJ, which also shows good consistency with our result. To compare Ce values in the same region, the Ce values in this data set within the near-fire source regions of above fire cases are extracted in Table 3. In the NEC and Siberia fires, the Ce values are in good consistency with the data set, while in California our result shows a much higher value. Pereira et al. (2009) found a Ce value of 30 g/MJ for the Amazon forest and Brazilian cerrado biomes and 20 g/MJ for Atlantic forest biomes in South America, which are less than the result presented in this study.

The NO_x Ce values derived by Mebust et al. (2011) in the California and Nevada range from 0.24 ± 0.07 to 0.61 ± 0.08 g/MJ, which are lower than our result from the California cases (0.84 ± 0.23 g/MJ). Moreover, they also obtained the mean Ce values for all biomes falling between 0.25 ± 0.03 and 0.36 ± 0.02 g/MJ (Mebust & Cohen, 2014). For different biomes, most of their emission coefficients are below 1.2 g/MJ. Our results are higher than their mean value but generally fall in their valid ranges. Good consistency is shown when compared with the prior work by Schreier et al. (2014), for in their study the Ce ranged from 0.28 to 1.56 g/MJ.

To the best of our knowledge, there are few Ce values of HCHO derived from satellite observations available. To objectively assess the current HCHO Ce, emission factors (EF, expressed as g/kg) collected from previous literature were converted into Ce values by simply multiplying by an energy-mass-conversion (EMC) factor, which is a constant for conversion from FRP to dry matter burned. In the current study, the EMC of 0.41 kg/MJ (Vermote et al., 2009) was adopted. The mean EF values of HCHO extracted from the previous

works (Andreae & Merlet, 2001; Wooster et al., 2011) range from 0.26 to 2.60 g/kg, and the corresponding converted Ce fall between 0.11 and 1.07 g/MJ, which is highly consistent with our results (0.55 ± 0.20–1.08- ± 0.21 g/MJ).

Ce values of CO retrieved from satellite observation are also rare in the literature. Freeborn et al. (2008) obtained the mean Ce values of CO from laboratory biomass fires by using two different middle infrared thermal imaging systems, determining values of 45.58 and 32.88 g/MJ. Andreae and Merlet (2001) listed a table of EF of various species including the CO with values ranging from 65 ± 20 to 107 ± 37 g/kg. The same as for HCHO, we converted the data into the expression expressed as g/MJ and obtained the corresponding values of 26.65 ± 8.2 to 43.87 ± 15.17 g/MJ. The Ce values in our results obtained from Siberia are significantly higher than these two results.

In conclusion, our results are in reasonable ranges and show good consistency with prior published research.

4.2. Possible Reasons for the Differences of Fire Emissions Among Cases

From the above analysis, we know that the fire case F1 features a strong FRP, low FRP-based aerosol emission rate, very high NO_x emission rate, and very low CO emission rate (refer to Figure 5) compared to those in forest fires in Siberia and California. Those noteworthy differences could be explained as follows.

First, the major biome types burned in F1 are cropland and woody savannas (Figure 1) rather than forest as in the other cases. F1 may have more thin branches and stems compared to trees in a forest (cases F2–F6), and this type of fuel (particularly with high near-surface wind speed as shown in Table 1) may favor fast combustion and thus release more FRP; that is, it has stronger fire intensity. However, the burned biomass of such a fire may be relatively lower than that burned in a forest; therefore, it released a smaller amount of aerosol for given FRP (i.e., weak fire severity). In addition, it is speculated that the crops and the soil underneath contain a high content of nitrogen due to agricultural fertilization. The nitrogen was released during the combustion process and led to a high emission rate and Ce of NO_x.

Fire emissions are highly related to fuel type in the literature. As Schreier et al. (2014) demonstrated, woody savanna and cropland fires have a relatively higher NO_x Ce than forest fires, and this could result from woody savanna and cropland biomes having higher N content than forests, providing more N content to be oxidized into NO_x. Meanwhile, for smoke aerosols, Vadrevu et al. (2015) pointed out that forest fires emitted more absorptive aerosols than cropland. Differences among fires in the current work showed good consistencies with their descriptions.

Second, the combustion phase is another major factor, which could affect the fire emissions remarkably. Mebust and Cohen (2014) mentioned that flaming combustion with a higher temperature than smoldering is believed to oxidize the N more effectively. Hardy et al. (2001) indicated that the amount of smoke particles emitted from per dry mass consumed in smoldering phases is more than double that of the flaming phase. Besides aerosols, CO is also efficiently produced by incomplete combustion (smoldering).

The cropland case F1 in NEC, with the highest Ce of NO_x and low Ce of aerosol and CO, may have a smaller smoldering proportion than the forest cases in Siberia and California. This is possible because (1) cropland and wood savannas have more thin branches and stems than a forest; thus, smoldering combustion is less prevalent (Hardy et al., 2001). (2) F1 occurred in October (the dry season), whereas the other cases were in June and July, the wet season. Vegetation in the dry season generally has a lower vegetation water content and burns more efficiently. And (3) smaller wind speed means less oxygen could be obtained, leading to higher percentage of smoldering.

4.3. The Direct Shortwave Radiative Forcing (DSRF) at TOA

Based on Figure 8, the absolute values of DSRF of this study vary from 0 to ~180 W/m^2 under different aerosol loadings in different cases. However, after being normalized by the associated AOD, the DSRF per unit AOD is very consistent among all cases (20.09 ± 0.89 to 22.93 ± 1.01 $Wm^{-2}\tau^{-1}$).

Santos et al. (2008) estimated the average DSRF efficiencies at TOA of forest fire smoke of 28 $Wm^{-2}\tau^{-1}$ and 33 $Wm^{-2}\tau^{-1}$ (550 nm) over two regions in Portugal. Christopher et al. (2000) retrieved the DSRF efficiencies ranging from 20 to 60 $Wm^{-2}\tau^{-1}$ in biomass burning smoke dominated region in South America. Patadia et al. (2008) obtained a 5-year mean value 44 $Wm^{-2}\tau^{-1}$ from biomass burning aerosol at TOA in

Amazonia. Compared with their results, the values in our works are slightly smaller but within their reasonable range.

The above results imply that there are large variations of fire intensity, fire emissions, and relative chemical compositions among individual fire cases, but the DSRF per unit AOD shows similar values, at least among our selected cases. Our results are generally consistent with those in the literature. This is a good sign that we can use the observed AOD in other fire cases to roughly estimate the induced DSRF. Of course, this speculation needs solid validation studies, particularly from long-term statistical studies.

5. Summary

The emissions of aerosol, trace gases, and the associated direct shortwave radiative forcing from multiple wildfires in the northeast of China (NEC), Siberia, Russia, and California, USA, with dominant fuel types of cropland, mixed forest, and needle-leaf forest, respectively, are studied based on state-of-the-art satellite observations. The FRP-based emission coefficients (Ce) of aerosol, NO_x (NO_2 + NO), formaldehyde (HCHO), and carbon monoxide (CO) were derived from combined products from Aqua Moderate-Resolution Imaging Spectroradiometer (MODIS), Aqua Atmospheric Infrared Sounder, Aura Ozone Monitoring Instrument (OMI), and AquaCloud's and the Earth's Radiant Energy System (CERES) using the method of Ichoku and Kaufman (2005). The cropland fire case in NEC featured relatively higher fire intensity (FRP), lower Ce of aerosol and CO emissions, and significantly higher Ce of NO_x emissions comparing to those in forest fire cases.

The relative chemical compositions of the smoke were examined by analyzing the relationships among different trace gas species and aerosols. Strong spatial correlations were found among aerosol optical depth (AOD), NO_x, HCHO, and CO. The three ratios of NO_x to AOD, HCHO, and CO in the cropland case in NEC show much higher values than those in other cases.

Although huge differences of fire intensity, fire emissions, and composition ratios were found among the cases of this study, the DSRF per AOD of smoke at the TOA showed good consistency, with the shortwave radiative forcing efficiency values of 20.09 $Wm^{-2}\tau^{-1}$, 21.62 $Wm^{-2}\tau^{-1}$, 22.93 $Wm^{-2}\tau^{-1}$, and 21.59 $Wm^{-2}\tau^{-1}$, respectively.

Our results reveal the noteworthy variations of the FRP-based emission coefficient and relative chemical composition, which might be due to the difference of biomes type burned, the combustion states (flaming or smoldering), and/or the weather conditions. Findings here would provide useful information to the estimation of fire emission and radiative forcing effect, and associated statistical study is undergoing.

Acknowledgments
All the data for this study are available at https://pan.baidu.com/s/1L74coAGwlruzaiaQUfisGQ. We appreciate the constructive comments and suggestions from three anonymous reviewers. This work was supported by the National Key Research and Development Program of China (grant 2017YFC1501402), Belmont Forum and JPI-Climate Collaborative Research Action with NSFC (grant 41661144007), National Natural Science Foundation of China NSFC (grants 41675022 and 41375148), the "Hundred Talents Program" of the Chinese Academy of Sciences, the "Hundred Talents Program" of Anhui Province, the Hefei Institute of Physical Science (grant 2014FXZY007), and the Jiangsu Provincial 2011 Program (Collaborative Innovation Center of Climate Change).

References

AIRS Science Team/Joao Texeira (2013). AIRS/Aqua L2 standard physical retrieval (AIRS+AMSU) V006, Greenbelt, MD, USA, Goddard Earth Sciences Data and Information Services Center (GES DISC), accessed on May 2017. https://doi.org/10.5067/AQUA/AIRS/DATA 201

Akagi, S. K., Yokelson, R. J., Wiedinmyer, C., Alvarado, M. J., Reid, J. S., Karl, T., et al. (2011). Emission factors for open and domestic biomass burning for use in atmospheric models. *Atmospheric Chemistry and Physics*, *11*(9), 4039–4072. https://doi.org/10.5194/acp-11-4039-2011

Andreae, M. O., & Merlet, P. (2001). Emission of trace gases and aerosols from biomass burning. *Global Biogeochemical Cycles*, *15*(4), 955–966. https://doi.org/10.1029/2000gb001382

Andreae, M. O., Rosenfeld, D., Artaxo, P., Costa, A. A., Frank, G. P., Longo, K. M., & Silva-Dias, M. A. F. (2004). Smoking rain clouds over the Amazon. *Science*, *303*(5662), 1337–1342. https://doi.org/10.1126/science.1092779

Bergeron, Y., & Gauthier, S. (Eds.) (2017). *Fire regimes: Spatial and temporal variability and their effects on forests*. St. Alban-anlage 66, 4052 Basel, Switzerland: Multidisciplinary Digital Publishing institute.

Christopher, S. A., Kliche, D. V., Chou, J., & Welch, R. M. (1996). First estimates of the radiative forcing of aerosols generated from biomass burning using satellite data. *Journal of Geophysical Research*, *101*(D16), 21,265–21,273. https://doi.org/10.1029/96jd02161

Christopher, S. A., Li, X., Welch, R. M., Reid, J. S., Hobbs, P. V., Eck, T. F., & Holben, B. (2000). Estimation of surface and top-of-atmosphere shortwave irradiance in biomass-burning regions during SCAR-B. *Journal of Applied Meteorology*, *39*(10), 1742–1753. https://doi.org/10.1175/1520-0450-39.10.1742

Crutzen, P. J., & Andreae, M. O. (1990). Biomass burning in the tropics: Impact on atmospheric chemistry and biogeochemical cycles. *Science*, *250*(4988), 1669–1678. https://doi.org/10.1126/science.250.4988.1669

De Smedt, I., Stavrakou, T., Hendrick, F., Danckaert, T., Vlemmix, T., Pinardi, G., et al. (2015). Diurnal, seasonal and long-term variations of global formaldehyde columns inferred from combined OMI and GOME-2 observations. *Atmospheric Chemistry and Physics*, *15*(21), 12,519–12,545. https://doi.org/10.5194/acp-15-12519-2015

Dee, D. P., Uppala, S. M., Simmons, A. J., Berrisford, P., Poli, P., Kobayashi, S., et al. (2011). The ERA-Interim reanalysis: Configuration and performance of the data assimilation system. *Quarterly Journal of the Royal Meteorological Society*, *137*(656), 553–597. https://doi.org/10.1002/qj.828

Freeborn, P. H., Wooster, M. J., Hao, W. M., Ryan, C. A., Nordgren, B. L., Baker, S. P., & Ichoku, C. (2008). Relationships between energy release, fuel mass loss, and trace gas and aerosol emissions during laboratory biomass fires. *Journal of Geophysical Research*, *113*, D01301. https://doi.org/10.1029/2007JD008679

Friedl, M. A., Sulla-Menashe, D., Tan, B., Schneider, A., Ramankutty, N., Sibley, A., & Huang, X. (2010). MODIS Collection 5 global land cover: Algorithm refinements and characterization of new datasets. *Remote Sensing of Environment*, *114*(1), 168–182. https://doi.org/10.1016/j.rse.2009.08.016

Giglio, L., Descloitres, J., Justice, C. O., & Kaufman, Y. J. (2003). An enhanced contextual fire detection algorithm for MODIS. *Remote Sensing of Environment*, *87*(2-3), 273–282. https://doi.org/10.1016/S0034-4257(03)00184-6

Giglio, L., & Justice, C. (2015). MYD14 MODIS/Aqua thermal anomalies/fire 5-min L2 swath 1km V006. NASA EOSDIS Land Processes DAAC. https://doi.org/10.5067/MODIS/MYD14.006

Goldammer, J. G., Davidenko, E. P., Kondrashov, L. G., & Ezhov, N. I. (2004). Recent trends of forest fires in Central Asia and opportunities for regional cooperation in forest fire management. In regional Forest congress "Forest policy: Problems and solutions (pp. 25-27).

Goldammer, J. G., Statheropoulos, M., & Andreae, M. O. (2008). Impacts of vegetation fire emissions on the environment, human health, and security: A global perspective. *Developments in Environmental Science*, *8*, 3–36. https://doi.org/10.1016/S1474-8177(08)00001-6

Hardy, C. C., Ottmar, R. D., Peterson, J. L., Core, J. E., & Seamon, P. (2001). Smoke management guide for prescribed and wildland fire: 2001 edition. PMS 420-2. NFES 1279. Boise, ID: National Wildfire Coodination Group. 226 p.

Hawbaker, T. J., Radeloff, V. C., Syphard, A. D., Zhu, Z., & Stewart, S. I. (2008). Detection rates of the MODIS active fire product in the United States. *Remote Sensing of Environment*, *112*(5), 2656–2664. https://doi.org/10.1016/j.rse.2007.12.008

Hawkins, L. N., & Russell, L. M. (2010). Oxidation of ketone groups in transported biomass burning aerosol from the 2008 northern California lightning series fires. *Atmospheric Environment*, *44*(34), 4142–4154. https://doi.org/10.1016/j.atmosenv.2010.07.036

Huijnen, V., Flemming, J., Kaiser, J. W., Inness, A., Leitão, J., Heil, A., et al. (2012). Hindcast experiments of tropospheric composition during the summer 2010 fires over western Russia. *Atmospheric Chemistry and Physics*, *12*(9), 4341–4364. https://doi.org/10.5194/acp-12-4341-2012

Ichoku, C., & Ellison, L. (2014). Global top-down smoke-aerosol emissions estimation using satellite fire radiative power measurements. *Atmospheric Chemistry and Physics*, *14*(13), 6643–6667. https://doi.org/10.5194/acp-14-6643-2014

Ichoku, C., & Kaufman, Y. J. (2005). A method to derive smoke emission rates from MODIS fire radiative energy measurements. *IEEE Transactions on Geoscience and Remote Sensing*, *43*(11), 2636–2649. https://doi.org/10.1109/Tgrs.2005.857328

Jaeglé, L., Steinberger, L., Martin, R. V., & Chance, K. (2005). Global partitioning of NO x sources using satellite observations: Relative roles of fossil fuel combustion, biomass burning and soil emissions. *Faraday Discussions*, *130*, 407–423. https://doi.org/10.1039/B502128F

Kaiser, J. W., Heil, A., Andreae, M. O., Benedetti, A., Chubarova, N., Jones, L., et al. (2012). Biomass burning emissions estimated with a global fire assimilation system based on observed fire radiative power. *Biogeosciences*, *9*(1), 527–554. https://doi.org/10.5194/bg-9-527-2012

Kaufman, Y. J., Justice, C. O., Flynn, L. P., Kendall, J. D., Prins, E. M., Giglio, L., et al. (1998). Potential global fire monitoring from EOS-MODIS. *Journal of Geophysical Research*, *103*(D24), 32,215–32,238. https://doi.org/10.1029/98JD01644

Kelly, C. (2007). OMI/Aura formaldehyde (HCHO) Total column 1-orbit L2 swath 13x24 km V003, Greenbelt, MD, USA, Goddard Earth Sciences Data And Information Services Center (GES DISC), accessed on September 2016. https://doi.org/10.5067/Aura/OMI/DATA 2015

Krotkov, N., & Veefkind, P. (2016). OMI/Aura nitrogen dioxide (NO_2) Total and tropospheric column 1-orbit L2 swath 13x24 km V003, greenbelt, MD, USA, Goddard earth sciences data and information services center (GES DISC) accessed on September 2016. https://doi.org/10.5067/Aura/OMI/DATA 2017

Krotkov, N. A., Lamsal, L. N., Celarier, E. A., Swartz, W. H., Marchenko, S. V., Bucsela, E. J., et al. (2017). The version 3 OMI NO 2 standard product. *Atmospheric Measurement Techniques*, *10*(9), 3133–3149. https://doi.org/10.5194/amt-10-3133-2017

Langmann, B., Duncan, B., Textor, C., Trentmann, J., & Van der Werf, G. R. (2009). Vegetation fire emissions and their impact on air pollution and climate. *Atmospheric Environment*, *43*(1), 107–116. https://doi.org/10.1016/j.atmosenv.2008.09.047

Li, R., Dong, X., Guo, J., Fu, Y., Wang, Y., & Min, Q. (2017). The implications of dust ice nuclei effect on cloud top temperature in a complex mesoscale convective system. *Scientific Reports*, *7*(1), 13826. https://doi.org/10.1038/s41598-017-12681-0

Li, R., Li, J., Liu, Z., Hua, J., Wang, Y., & Wang, W. (2016). Satellite observational study on correlations among aerosol optical depth, NO_2 and SO_2 over China. *Chinese Science Bulletin*, *61*(22), 2524–2535. https://doi.org/10.1360/N972016-00149

Li, R., & Min, Q. L. (2010). Impacts of mineral dust on the vertical structure of precipitation. *Journal of Geophysical Research*, *115*, D09203. https://doi.org/10.1029/2009JD011925

Li, R., Min, Q. L., & Harrison, L. C. (2010). A case study: The indirect aerosol effects of mineral dust on warm clouds. *Journal of the Atmospheric Sciences*, *67*(3), 805–816. https://doi.org/10.1175/2009JAS3235.1

Loeb, N. G., Kato, S., Loukachine, K., Manalo-Smith, N., & Doelling, D. R. (2007). Angular distribution models for top-of-atmosphere radiative flux estimation from the clouds and the Earth's radiant energy system instrument on the Terra satellite. Part II: Validation. *Journal of Atmospheric and Oceanic Technology*, *24*(4), 564–584. https://doi.org/10.1175/JTECH1983.1

McMillan, W. W., Evans, K. D., Barnet, C. D., Maddy, E. S., Sachse, G. W., & Diskin, G. S. (2011). Validating the AIRS version 5 CO retrieval with DACOM in situ measurements during INTEX-A and-B. *IEEE Transactions on Geoscience and Remote Sensing*, *49*(7), 2802–2813. https://doi.org/10.1109/TGRS.2011.2106505

Mebust, A. (2013). Variability in wildfire emissions of nitrogen oxides as observed from space.

Mebust, A. K., & Cohen, R. C. (2014). Space-based observations of fire NO_x emission coefficients: A global biome-scale comparison. *Atmospheric Chemistry and Physics*, *14*(5), 2509–2524. https://doi.org/10.5194/acp-14-2509-2014

Mebust, A. K., Russell, A. R., Hudman, R. C., Valin, L. C., & Cohen, R. C. (2011). Characterization of wildfire NO_x emissions using MODIS fire radiative power and OMI tropospheric NO_2 columns. *Atmospheric Chemistry and Physics*, *11*(12), 5839–5851. https://doi.org/10.5194/acp-11-5839-2011

Meyer-Arnek, J., Ladstatter-Weissenmayer, A., Richter, A., Wittrock, F., & Burrows, J. P. (2005). A study of the trace gas columns O_3, NO_2 and HCHO over Africa in September 1997. *Faraday Discussions*, *130*, 387–405. https://doi.org/10.1039/b502106p

Min, Q., & Li, R. (2010). Longwave indirect effect of mineral dusts on ice clouds. *Atmospheric Chemistry and Physics*, *10*(16), 7753–7761. https://doi.org/10.5194/acp-10-7753-2010

Min, Q. L., Li, R., Lin, B., Joseph, E., Morris, V., Hu, Y., et al. (2014). Impacts of mineral dust on ice clouds in tropical deep convection systems. *Atmospheric Research*, *143*, 64–72. https://doi.org/10.1016/j.atmosres.2014.01.026

Min, Q. L., Li, R., Lin, B., Joseph, E., Wang, S., Hu, Y., et al. (2009). Evidence of mineral dust altering cloud microphysics and precipitation. *Atmospheric Chemistry and Physics*, *9*(9), 3223–3231. https://doi.org/10.5194/acp-9-3223-2009

OMI Team (2012). *Ozone Monitoring Instrument (OMI) Data user's Guide*. Washington DC: NASA.

Oris, F., Asselin, H., Ali, A. A., Finsinger, W., & Bergeron, Y. (2013). Effect of increased fire activity on global warming in the boreal forest. *Environmental Reviews*, *22*(3), 206–219. https://doi.org/10.1139/er-2013-0062

Patadia, F., Gupta, P., Christopher, S. A., & Reid, J. S. (2008). A multisensor satellite-based assessment of biomass burning aerosol radiative impact over Amazonia. *Journal of Geophysical Research*, *113*, D12214. https://doi.org/10.1029/2007JD009486

Pereira, G., Freitas, S. R., Moraes, E. C., Ferreira, N. J., Shimabukuro, Y. E., Rao, V. B., & Longo, K. M. (2009). Estimating trace gas and aerosol emissions over South America: Relationship between fire radiative energy released and aerosol optical depth observations. *Atmospheric Environment*, *43*(40), 6388–6397. https://doi.org/10.1016/j.atmosenv.2009.09.013

Reid, J. S., Eck, T. F., Christopher, S. A., Koppmann, R., Dubovik, O., Eleuterio, D. P., et al. (2005). A review of biomass burning emissions. Part III: Intensive optical properties of biomass burning particles. *Atmospheric Chemistry and Physics*, *5*(3), 827–849. https://doi.org/10.5194/acp-5-827-2005

Santos, D., Costa, M. J., & Silva, A. M. (2008). Direct SW aerosol radiative forcing over Portugal. *Atmospheric Chemistry and Physics*, *8*(19), 5771–5786. https://doi.org/10.5194/acp-8-5771-2008

Schreier, S. F., Richter, A., Kaiser, J. W., & Burrows, J. P. (2014). The empirical relationship between satellite-derived tropospheric NO_2 and fire radiative power and possible implications for fire emission rates of NO_x. *Atmospheric Chemistry and Physics*, *14*(5), 2447–2466. https://doi.org/10.5194/acp-14-2447-2014

Torres, O. O. (2006). OMI/Aura near UV aerosol optical depth and single scattering albedo 1-orbit L2 swath 13x24 km V003, Greenbelt, MD, USA, Goddard Earth Sciences Data and Information Services Center (GES DISC), Accessed on September2016. https://doi.org/10.5067/Aura/OMI/DATA 2004

Vadrevu, K. P., Lasko, K., Giglio, L., & Justice, C. (2015). Vegetation fires, absorbing aerosols and smoke plume characteristics in diverse biomass burning regions of Asia. *Environmental Research Letters*, *10*(10), 105003. https://doi.org/10.1088/1748-9326/10/10/105003

Van Leeuwen, T. T., & Van Der Werf, G. R. (2011). Spatial and temporal variability in the ratio of trace gases emitted from biomass burning. *Atmospheric Chemistry and Physics*, *11*(8), 3611–3629. https://doi.org/10.5194/acp-11-3611-2011

Veefkind, J. P., Boersma, K. F., Wang, J., Kurosu, T. P., Krotkov, N., Chance, K., & Levelt, P. F. (2011). Global satellite analysis of the relation between aerosols and short-lived trace gases. *Atmospheric Chemistry and Physics*, *11*(3), 1255–1267. https://doi.org/10.5194/acp-11-1255-2011

Verma, S., Worden, J., Pierce, B., Jones, D., Al-Saadi, J., Boersma, F., et al. (2009). Ozone production in boreal fire smoke plumes using observations from the tropospheric emission spectrometer and the Ozone Monitoring Instrument. *Journal of Geophysical Research*, *114*, D02303. https://doi.org/10.1029/2008JD010108

Vermote, E., Ellicott, E., Dubovik, O., Lapyonok, T., Chin, M., Giglio, L., & Roberts, G. J. (2009). An approach to estimate global biomass burning emissions of organic and black carbon from MODIS fire radiative power. *Journal of Geophysical Research*, *114*, D18205. https://doi.org/10.1029/2008JD011188

Wang, X., Liu, J., Che, H. Z., Ji, F., & Liu, J. J. (2018). Spatial and temporal evolution of natural and anthropogenic dust events over northern China. *Scientific Reports*, *8*, 2141. https://doi.org/10.1038/s41598-018-20382-5

Wang, X., Wen, H., Shi, J., Bi, J., Huang, Z., Zhang, B., et al. (2018). Optical and microphysical properties of natural mineral dust and anthropogenic soil dust near dust source regions over northwestern China. *Atmospheric Chemistry and Physics*, *18*(3), 2119–2138. https://doi.org/10.5194/acp-18-2119-2018

Wielicki, B. A., Barkstrom, B. R., Harrison, E. F., Lee, R. B. III, Louis Smith, G., & Cooper, J. E. (1996). Clouds and the Earth's Radiant Energy System (CERES): An earth observing system experiment. *Bulletin of the American Meteorological Society*, *77*(5), 853–868. https://doi.org/10.1175/1520-0477(1996)077<0853:CATERE>2.0.CO;2

Wooster, M. J., Freeborn, P. H., Archibald, S., Oppenheimer, C., Roberts, G. J., Smith, T. E. L., et al. (2011). Field determination of biomass burning emission ratios and factors via open-path FTIR spectroscopy and fire radiative power assessment: Headfire, backfire and residual smouldering combustion in African savannahs. *Atmospheric Chemistry and Physics*, *11*(22), 11,591–11,615. https://doi.org/10.5194/acp-11-11591-2011

Yokelson, R. J., Bertschi, I. T., Christian, T. J., Hobbs, P. V., Ward, D. E., & Hao, W. M. (2003). Trace gas measurements in nascent, aged, and cloud-processed smoke from African savanna fires by airborne Fourier transform infrared spectroscopy (AFTIR). *Journal of Geophysical Research*, *108*(D13), 8478. https://doi.org/10.1029/2002JD002322